Emergent magnetic order in the antiferromagnetic Kitaev model in a [111] field

Will Holdhusen [1], Daniel Huerga [2], and Gerardo Ortiz [1,3]

[1]*Department of Physics, Indiana University, Bloomington, Indiana 47405, USA*
[2]*Stewart Blusson Quantum Matter Institute, University of British Columbia, Vancouver, British Columbia V6T 1Z4, Canada*
[3]*Institute for Quantum Computing, University of Waterloo, Waterloo, Ontario N2L 3G1, Canada*

The Kitaev spin liquid, stabilized as the ground state of the Kitaev honeycomb model, is a paradigmatic example of a topological $\mathbb{Z}_2$ quantum spin liquid. The fate of the Kitaev spin liquid in presence of an external magnetic field is at present, a subject of intense scrutiny due to recent experimental signatures pointing to a $\mathbb{Z}_2$ topological phase in certain materials, as well as theoretical studies predicting the emergence of a quantum spin liquid phase of debated nature. In this work, we employ hierarchical mean-field theory, a method based on the use of clusters preserving relevant symmetries and short-range quantum correlations, to investigate the quantum phase diagram of the antiferromagnetic Kitaev's model in a [111] magnetic field. By using clusters of 24 sites, we predict that the Kitaev spin liquid transits through two intermediate phases, characterized by emerging stripe and chiral orders, respectively, before entering the trivial partially polarized phase, differing from previous studies. We assess our results by performing exact diagonalization and computing the scaling of different observables, including the many-body Chern number and other topological quantities, thus establishing hierarchical mean-field theory as a method to study models of frustrated quantum magnetism potentially hosting topological quantum spin liquids.

I. INTRODUCTION

Quantum spin liquids (QSLs) are featureless phases of matter resulting from competing interactions among elementary magnetic degrees of freedom. While no consensus exists on the precise operational characterization of a QSL, commonly accepted defining properties include translational and rotational invariance, the absence of long-range (Landau) magnetic order, and incipient topological order [1,2]. Perhaps the most agreed-upon example of a QSL is found in the ground state of the Kitaev honeycomb model (KHM) [3]. This model, with an exact solution in terms of Majorana fermions coupled to a $\mathbb{Z}_2$ gauge field [3,4], provides an archetypal example of a topological $\mathbb{Z}_2$ QSL (the Kitaev spin liquid, KSL) hosting non-Abelian anyonic low-lying excitations, thus constituting a potential resource for quantum information processing. Given the seemingly unphysical interactions constituting the KHM, indications that physical realizations may be possible in the so-called Kitaev materials are surprising. While these materials, most famously $\alpha - RuCl_3$, exhibit antiferromagnetic ordering, an applied magnetic field suppresses the order and uncovers KSL-like fractionalization [5–7]. Importantly, interactions beyond those in Kitaev's exactly solvable Hamiltonian are also present in these materials [8–11].

The growth of this field has led to further interest in the fate of the KSL outside of its exactly solvable regime [12–20]. Recent numerical simulations have shown that even the simple application of a uniform magnetic field to the antiferromagnetic KHM leads to an unexpected result: the KSL persists up to a relatively high field strength and, in addition, a featureless QSL phase emerges before its transition into a trivial partially polarized phase. The ultimate nature of this intermediate phase is matter of current debate [21,22].

The simple addition of a magnetic field takes the KHM out of its exactly solvable regime, necessitating either numerical or mean-field approaches. The majority of studies on the effect of [111] (out-of-plane) magnetic fields have focused on results derived from exact-diagonalization (ED) [21,23–25] and density-matrix renormalization group (DMRG) calculations [21,22,25,26]. Calculations with both approaches seem to consistently predict a gapless $U(1)$ QSL in the intermediate phase. However, variational calculations based on an effective mean-field theory over the Majorana fermion degrees of freedom capturing the zero field (exactly solvable) regime have suggested that this intermediate phase is a gapped topological QSL belonging to Kitaev's 16-fold way with Chern number $C = 4$ [27], in agreement with a prediction from variational Monte Carlo [28]. In addition, a distinct topological intermediate phase with $C = -2$ has been suggested to occur under the application of in-plane magnetic fields [29,30]. As each method techniques used to study this model suffers from its own biases and limitations, a comprehensive understanding of the true quantum phase diagram thus requires a holistic approach combining information from multiple sources.

Here, we provide an augmenting perspective by approaching the problem with hierarchical mean-field theory (HMFT), a method based on the identification of cluster degrees of freedom preserving relevant symmetries and quantum correlations of the Hamiltonian [31–33]. HMFT provides a simulation of the thermodynamic limit and a variational upper bound to the exact ground state energy, approaching the exact result through finite-scaling analysis with increasing cluster size [34]. HMFT has proven successful in recovering the phase diagram of systems with competing long-range orders (LROs)
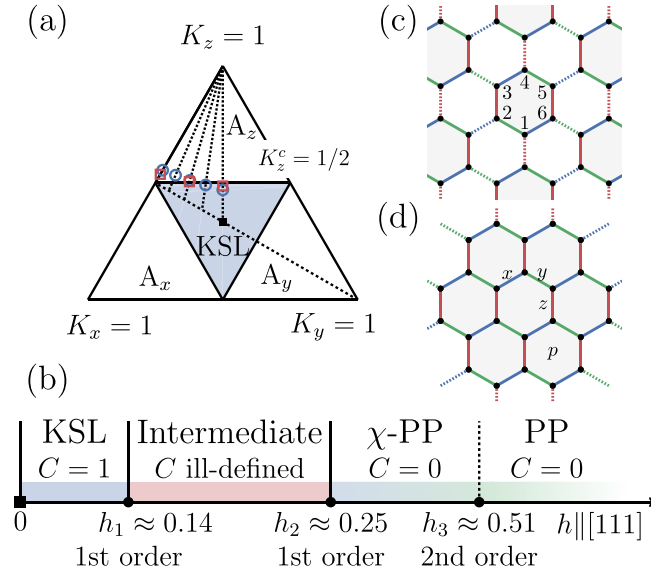
FIG. 1. (a) Quantum phase diagram of the KHM as obtained with 6- and 24-site HMFT (blue circles and red squares, respectively) as compared to the exact solution (continuous black). (b) Schematic quantum phase diagram of the KHM at $K_x = K_y = K_z = 1$ under an external magnetic field h along the [111] direction [Eq. (1)] as obtained with HMFT and ED, including the Kitaev spin liquid (KSL), intermediate, and chiral and trivial partially polarized phases (χ-PP and PP, respectively). Phase boundaries correspond to 24-site HMFT results and Chern numbers C have been computed with 24-site ED. Comparison of our results to those in references [14,23] requires rescaling our magnetic field as $h \rightarrow \sqrt{3}h$. (c) Cluster used for 6-site HMFT. Indexing corresponds to the plaquette flux W_p [Eq. (2)]. (d) Cluster used for 24-site HMFT with KHM bond directions labeled. The index p indicates the center of one of the plaquettes on which W_p is defined.

and quantum paramagnetic phases [34–36], including the prediction of a devil's staircase of valence-bond crystals in the kagome Heisenberg antiferromagnet [37] confirmed in later experiments [38].

The present work represents the first application of HMFT to a model hosting topological order. We begin by simulating the exactly solvable KHM to assess our approach, obtaining a phase diagram in good agreement with the exact solution as shown in Fig. 1(a). Then, we uncover the phase diagram upon application of a magnetic field along the [111] direction [Fig. 1(b)] and utilize ED to provide support to our new results. While HMFT confirms the presence of an intermediate phase appearing in a [111] field, the phase diagram obtained has important distinctions from earlier results.

First, we find that the intermediate phase spontaneously breaks the rotational symmetry of the KHM Hamiltonian, with the broken symmetry caused by competition between different mean-field configurations representing local minima of the HMFT energy. In this phase, we find results suggestive of long-range order (LRO) in the form of stripy antiferromagnetism rather than the featurelessness characteristic of a QSL, per its usual definition [1,2]. Second, we find a chiral partially polarized (χ-PP) phase occurring between the intermediate and the trivial partially polarized (PP) phases. The χ-PP phase

has gone unnoticed in previous studies based on ED [21,23–25] and DMRG [21,22,25,26]. This newly uncovered phase is characterized by a sublattice chiral order parameter and is separated from the PP phase by a second-order phase transition.

The remainder of this introduction outlines the organization of the manuscript. We first review the exactly solvable Kitaev honeycomb model (KHM) at zero field in Sec. II and the methods used (HMFT and ED) in Sec. III. In Sec. IV, we present our results on the HMFT approach to the KHM in a [111] field, making particular emphasis on our new results: the emergence of stripe order in the intermediate phase and the novel χ-PP phase. In this section, we also make use of ED to assess the validity of the HMFT results. Finally, in Sec. V we conclude with remarks examining the consequences of our study and opportunities for future work building on and further testing the resulting predictions.

II. MODEL

The $S = 1/2$ KHM [3], $H = \sum_\gamma \sum_{\langle i,j \rangle^\gamma} K_\gamma S_i^\gamma S_j^\gamma$, characterized by bond-dependent nearest-neighbor $\langle i, j \rangle^\gamma$ ($\gamma \in \{x, y, z\}$) interactions, is the paradigmatic model stabilizing QSL phases characterized by topological order. Its exact solution is recovered upon mapping the $S = 1/2$ spins to Majorana fermions coupled to a $\mathbb{Z}_2$ gauge field [3,4]. Its implications to quantum computation have made the search for Kitaev interactions in materials a consequential line of research. Upon applying an external magnetic field h along the [111] direction to the KHM,

$$H = \sum_\gamma \sum_{\langle i,j \rangle^\gamma} K_\gamma S_i^\gamma S_j^\gamma - h \sum_i \left(S_i^x + S_i^y + S_i^z \right), \quad (1)$$

Kitaev showed that a gap opens for $h \ll 1$, revealing a topological nontrivial ground state characterized by Chern number $C = \pm 1$ in the KSL phase, thus making the system a resource for topological quantum computation via the braiding of its non-Abelian anyon excitations [3].

At $h = 0$, a set of plaquette observables (sometimes referred to as the "plauqette flux") defined on the dual lattice, i.e., at each 6-site hexagon p of the honeycomb lattice [see Fig. 1(c)],

$$W_p = 2^6 S_1^z S_2^x S_3^y S_4^z S_5^x S_6^y, \quad (2)$$

commutes with the Hamiltonian (1), rendering it exactly solvable. In the ground state, these observables have a well-defined value of $\langle W_p \rangle = 1$ for all plaquettes in the lattice [3]. The quantum phase diagram of the model comprises four phases: three gapped phases with Chern number $C = 0$ hosting Abelian anyons (dubbed A_γ), which occur for $|K_\gamma| > |K_\alpha| + |K_\beta|$, with $\{\alpha, \beta, \gamma\} \in \{x, y, z\}$, and a gapless (at $h = 0$) phase (the KSL or B phase), otherwise. Application of a perturbative magnetic field $h > 0$ opens a gap, revealing non-Abelian anyons and a Chern number $C = 1$ [3]. Figure 1(a) illustrates this phase diagram projected onto the surface defined by $K_x + K_y + K_z = 1$.

The transition from the topological KSL phase towards a trivial partially polarized phase (PP) emerging at large magnetic fields h is currently under scrutiny. Specifically, recent numerical analysis of the antiferromagnetic ($K_\gamma > 0$) KHM has argued for the existence of an intermediate, finite-field

QSL phase whose fundamental nature is under debate, occurring between the KSL and the trivial partially polarized phase at high fields. Recent studies based on different numerical approaches have argued in favor of a gapless $U(1)$ QSL [21–26] or a topological and gapped QSL characterized by a Chern number $C = 4$ [27,28].

We now briefly discuss the real-space symmetries of the KHM spontaneously broken by the first intermediate phase. Due to its anisotropic bond-dependent interactions, the KHM does not preserve the C_6 rotational symmetry of the honeycomb lattice. Even for the most symmetric set of couplings ($K_x = K_y = K_z$, occurring in the KSL phase), a rotation of the lattice by $\pi/3$ about the center of an hexagon (C_6) must be accompanied by a $2\pi/3$ rotation of the Bloch sphere about the [111] axis (C_3^S), resulting in a combined $C_6 \times C_3^S$ symmetry.[1] This remains a symmetry of the model under the application of a magnetic field, as long as it is applied in the [111] direction.

III. METHODS

A. Hierarchical mean-field theory

Hierarchical mean-field theory (HMFT) is an algebraic framework and numerical method to approach models of strongly correlated systems with frustrating interactions. The main idea of the method builds upon the identification of relevant degrees of freedom (generally, clusters of the original degrees of freedom) containing the necessary quantum correlations required to unveil the phases emerging in the system under study. By utilizing the exact mappings relating the algebras of the original and new degrees of freedom, we may encounter emerging symmetries and exact solutions [40] or, in their absence, utilize mean-field approaches [31–33]. Under the assumption that deep within a noncritical phase, the characteristic correlation length has a finite length of few sites, we generically make use of clusters containing N_c sites that uniformly tile the lattice and preserve as many symmetries of the original Hamiltonian as possible. Thus, quantum correlations within the cluster are described from the onset, while the remaining interactions among clusters may be approximated by different mean-field approaches.

The lowest-order mean-field approximation consists of a simple product of clusters, i.e., a uniform cluster-Gutzwiller ansatz (CGA),

$$|\Psi\rangle = \bigotimes_{\mathbf{R}} |\psi_{\mathbf{R}}\rangle, \tag{3}$$

where clusters at superlattice sites $\mathbf{R}$ are in the same state, $|\psi_{\mathbf{R}}\rangle = \sum_{\{\sigma\}} w_{\{\sigma\}} |\{\sigma\}\rangle$, and $w_{\{\sigma\}}$ are variational parameters in the basis of spin configurations of the cluster, $\{\sigma\}$. These variational parameters are optimized upon minimization of the energy density in the thermodynamic limit,

$$e = \frac{1}{MN_c} \frac{\langle\Psi|H|\Psi\rangle}{\langle\Psi|\Psi\rangle}, \tag{4}$$

where M is the total number of clusters in the superlattice (generally taken to be infinite). From a technical standpoint, minimization of Eq. (4) is equivalent to performing ED on a single cluster with open boundary conditions (OBC) embedded in a bath of self-consistently defined mean fields [34]. In tensor-network language, the CGA Eq. (3) is equivalent to a tree-tensor network with a single multi-qubit isometry with constraint $\sum_{\{\sigma\}} w_{\{\sigma\}}^* w_{\{\sigma\}} = 1$ [41,42].

The CGA energy (4) on finite clusters provides an upper bound to the ground state energy of the model in its thermodynamic limit. Inspection of derivatives of the CGA energy unveils the phase diagram. In addition, a finite-size scaling analysis allows the assessment of the stability of phases upon increasing the cluster size N_c and allows extrapolation of the location of phase boundaries. In this manner, the CGA provides a computationally inexpensive ansatz to approach models of frustrated quantum magnetism [43] that pose problems to state-of-the-art numerical approaches [44,45].

This simple yet expressive approximation has been applied to a variety of models where frustrated spin and bosonic interactions lead to the coexistence and competition of LRO and quantum paramagnetic phases, including valence-bond solids and chiral states [34–37,46]. The algebraic framework of HMFT allows for other self-consistent mean-field approximations, including a Bogoliubov approximation that enables the study of low-lying excitations [34] such as Goldstone and Higgs modes in superfluids [47]. Moreover, HMFT can be extended to investigate finite-temperature phase transitions [48] and to construct parent Hamiltonians of valence-bond solids [49].

Here, we utilize clusters of size $N_c = 6$ and 24 (see Fig. 1), representing the two minimal instances preserving the C_6 rotational symmetry of the honeycomb lattice, and systematically inspect the CGA energy and its derivatives to unveil the phase diagram of the KHM. We use the resulting CGA wave functions (3) to compute observables characterizing the emergence of LRO, or lack thereof, within the phases thus obtained. In addition we compute topological observables, such as the plaquette flux (2) and the topological entanglement entropy [50].

B. Exact diagonalization

We make extensive use of exact-diagonalization (ED) to support predictions arrived at through our HMFT simulations. Specifically, we utilize the Lanczos method as implemented in the QuSpin package [51] to find energy and wave functions for the ground state and low-lying excitations using clusters of size $N_c = 18$ and 24 with periodic boundary conditions (PBC) (see Fig. 2). We use these results to obtain quantities that can indicate the emergence of QSLs or other topologically ordered states, including the many-body Chern number [52–56] and the topological S matrix [57].

IV. PHASE DIAGRAM

A. Benchmarking HMFT at $h = 0$

To assess the validity of an HMFT description of QSL physics, we begin by studying the antiferromagnetic KHM

---

[1] Aligning the spin axes along real-space directions (such that a lattice rotation also rotates the spins) results in a different symmetry classification [39].
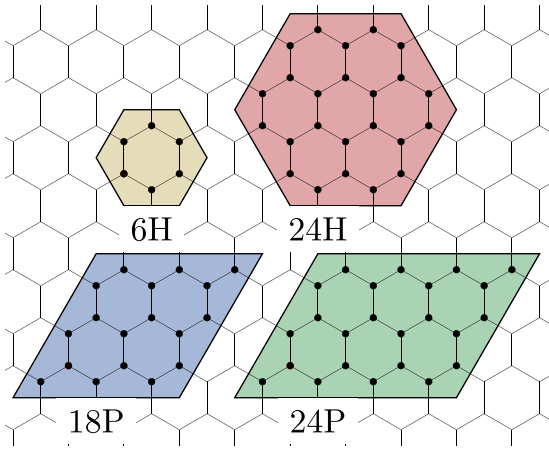
FIG. 2. Clusters used in exact-diagonalization with periodic boundary conditions. 6H and 24H clusters are identical to those used in HMFT calculations. 18P and 24P clusters are used for finite-size scaling analysis.

given by Eq. (1) at $h = 0$. This allows for direct comparison between HMFT results and those found via the model's exact solution [3].

Using 6- and 24-site CGA, HMFT provides a quantitatively accurate approximation of the exact phase diagram. In spite of the lack of a bulk in the 6-site cluster, HMFT on this cluster provides a qualitative picture of the boundaries between the A_γ and KSL phases that becomes more accurate upon increasing the cluster size to $N_c = 24$. The quality of even the 6-site results are unsurprising given the very short correlation length characteristic of the pure KHM [58].

In Fig. 1(a), we show 6- and 24-site HMFT results on the quantum phase diagram of the KHM at $h = 0$ along various cuts at fixed ratios of K_y/K_x. By inspecting discontinuities in the derivatives of the energy (4), we identify a weakly first-order transition from A_γ to KSL with 6-site HMFT that smoothes to second-order on the 24-site cluster, consistent with exact results (details are presented in Appendix A). Plaquette flux (2) computed with 6-site HMFT shows $W_p = -1$ for the intra-cluster plaquette, while the correct result $W_p = 1$ is recovered in 24-site HMFT for *all* intra-cluster plaquettes.[2] Additionally, topological entanglement entropy computed in the 24-site HMFT matches the exact solution [3], with $S_{\text{topo}} = -\log 2$ to within $\approx 10^{-5}$ throughout the entire $h = 0$ phase diagram.

At $K_x = K_y = K_z$, we find a ground state degeneracy corresponding to different embedding mean-field configurations reflecting magnetic orders not found in the exact solution. Specifically, while the unique 6-site mean-field solution has all nearest neighbor spins aligned in opposite directions (Néel order), the 24-site cluster allows for four categories of mean-field configuration characterized by either Néel or stripe magnetic order and varying rotational symmetry. We refer to these as the C_6-stripy, C_2-stripy, C_3-Néel, and C_2-Néel configurations, as illustrated in Fig. 3. Taking into account global

---

[2]As the CGA wave function substitutes mean fields for intercluster quantum correlations, $W_p = 0$ for intercluster plaquettes.

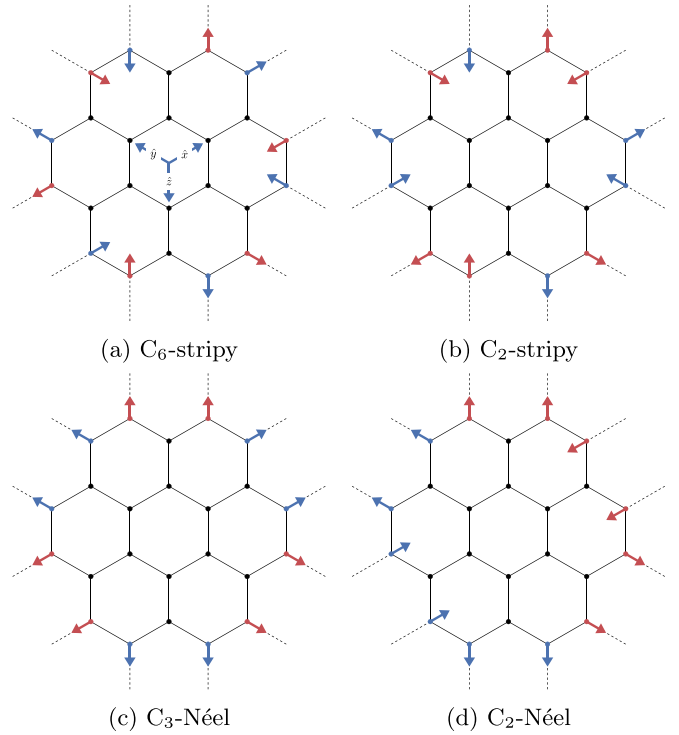(a) C_6-stripy   (b) C_2-stripy

(c) C_3-Néel   (d) C_2-Néel

FIG. 3. Expectation value of spin $\langle \vec{S}_i \rangle$ for the four mean-field configurations degenerate at $h = 0$ and $K_x = K_y = K_z$, with the mean-field configurations labeled by their symmetry and magnetic order. Arrows indicate values of the spin operators projected onto the plane perpendicular to the [111] direction [with positive directions depicted in (a)], with black dots indicating sites with zero expectation value. As a visual aid, blue (red) arrows indicate a positive (negative) expectation value in the [111] direction.

rotations and sign flips, this leads to a total of 16 distinct configurations with identical energy. Note that although LRO is generically concomitant to a nonzero mean-field embedding in CGA [Eq. (3)] [34,36,47], in this case, spins located within the bulk of the 24-site cluster are completely paramagnetic, $\langle \mathbf{S}_i \rangle = 0$. This causes the overall LRO signal to fall off as the ratio of cluster boundary to area with increasing cluster size, i.e., $\mathcal{O}(1/N_c)$. Therefore, the "mean-field magnetic order" appearing in the KSL is distinct from the LRO that we detect at $h \neq 0$, to be discussed in the remainder of this work. As we will see, true LRO in HMFT is a property permeating the bulk of the cluster, and thereby persists in the $N_c \to \infty$ limit. Further discussion of the different mean-field configurations is presented in Appendix B.

B. Kitaev honeycomb model in a [111] field

We now focus on the finite field region $h > 0$, for which no exact solution exists, and fix $K_x = K_y = K_z = 1$ and $h \parallel [111]$, thus preserving the maximal symmetry of the KHM (1) and placing the ground state at $h \ll 1$ deep within the the KSL phase. To characterize magnetic order, we compute the magnetization along the [111] direction, $M^{[111]} = 1/(N_c\sqrt{3}) \sum_{i,\gamma} \langle S_i^\gamma \rangle$, and the sublattice scalar chirality,

$$\chi_{ijk} = 2^3 \langle \mathbf{S}_i \cdot (\mathbf{S}_j \times \mathbf{S}_k) \rangle, \tag{5}$$

where i, j, and k are next-nearest neighbors on the honeycomb lattice forming a counter-clockwise cycle. Here and in all following equations, sums over the index i are confined to the N_c spins within a single cluster and all expectation values are taken with respect to the CGA wave function [Eq. (3)] in HMFT calculations and with respect to the ground state of the clusters with PBC (Fig. 2), in ED calculations. We define an average *staggered* sublattice chiral observable as

$$\overline{\chi}_{\text{stag}} = \frac{1}{N_c} \sum_{\langle\langle ijk \rangle\rangle} s_{ijk} w_{ijk} \chi_{ijk}, \tag{6}$$

where $\langle\langle ijk \rangle\rangle$ refers to next-nearest-neighbor sites of the honeycomb lattice (i.e., nearest neighbors on a sublattice), signs s_{ijk} are set equal to $+1$ (-1) for plaquette- (site-) centered triangles (thus accounting for the staggering of chiral currents common to triangular-lattice systems [17,59]), and weights w_{ijk} take into account the cluster tiling of the lattice, i.e., $w_{ijk} = 1, 1/2$, and $1/3$, for sites i, j, k belonging to one, two, or three clusters, respectively.

We also compute the expectation value of the plaquette flux operator (2) at every plaquette and define its average over the whole lattice,

$$\overline{W} = \frac{1}{N_c} \sum_p w_p \langle W_p \rangle, \tag{7}$$

where, similar to the chiral order parameter, the weight factors w_p take into account whether the operator acts on one ($w_p = 1$), two ($w_p = 1/2$), or three ($w_p = 1/3$) clusters.

Remark that due to the structure of the uniform CGA wave function (3), the expectation value of local operators acting on sites belonging to multiple clusters decomposes as products of expectation values of local local operators within each cluster. This implies that Eqs. (6) and (7) can be easily evaluated using the wave function of a single cluster, i.e., $|\psi_{\mathbf{R}}\rangle$ (see details in Appendix C).

To describe the topological character of QSLs, we compute the topological entanglement entropy S_{topo} via the Kitaev-Preskill construction [50] on the 24-site HMFT. Lack of a "bulk" (spins isolated from the cluster boundaries) in the 6-site cluster prevents computation of S_{topo} with this cluster in HMFT. Details of this calculation are covered in Appendix D.

Figure 4 illustrates our main results. First, we find a low-field KSL phase adiabatically connected to the exact $h = 0$ point, characterized by a positive average plaquette flux and topological entanglement entropy that decrease upon increasing h. This KSL ends at a first order transition, leading to an intermediate phase exhibiting enhanced stripe magnetization along a preferred axis. Before reaching the trivial partially polarized (PP) phase with nearly saturated [111] magnetization, we find a novel second intermediate phase characterized by the coexistence of finite scalar chirality (6) and partial polarization (thus χ-PP).

Interestingly, the phase diagram can be broadly understood as two consecutive level crossings occurring between the C_6- and C_2-stripy solutions, shown in Figs. 4(c) and 4(d). Specifically, the nonzero magnetic field breaks the aforementioned degeneracy at $h = 0$ in favor of the C_6-stripy solution within the KSL at finite h. At $h_1 \approx 0.14$, the C_2-stripy energy crosses below the C_6-stripy solution, becoming
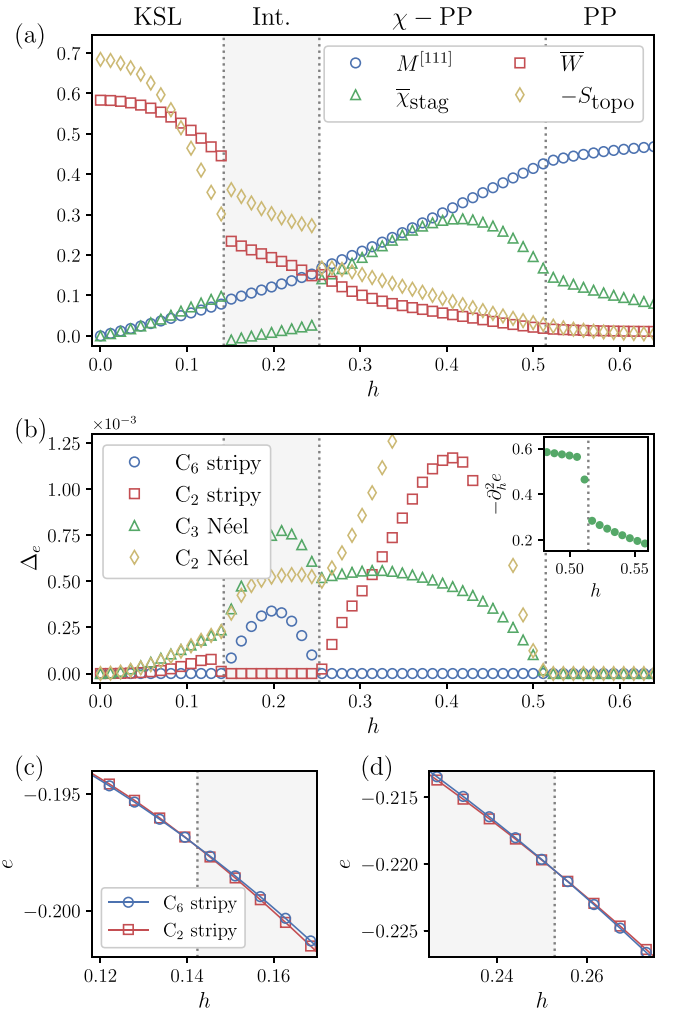

FIG. 4. (a) Magnetization, staggered chiral order parameter (6), average plaquette flux (7), and topological entanglement entropy as computed with 24-site HMFT. (b) Gaps of the lowest-lying competing HMFT solutions computed with respect to the optimal HMFT ground state energy. Inset: second derivative of the energy showing a discontinuity at h_3. (c), (d) Level crossings between the C_6- and C_2-stripy HMFT solutions at h_1 and h_2, respectively.

the new ground state of this intermediate phase and causing a first-order transition, albeit a subtle one due to the small difference in energy, as can be seen from the gap of order 10^{-3} in Fig. 4(b). At $h_2 \approx 0.25$, the situation reverses itself and the C_6-stripy solution crosses again, stabilizing the χ-PP phase. At $h_3 \approx 0.51$, we observe a continuous (second-order) phase transition towards the trivial PP phase signalled by a large discontinuity in $\partial_h^2 e$. At precisely this point, the C_2 and C_6-stripy solutions (along with the Néel-ordered solutions also degenerate at $h = 0$) lose their distinction when their mean-field parameters converge to identical values. Comparing these results with those obtained in previous ED [21,23–25] and DMRG [21,22,25,26] computations, 24-site HMFT predicts lower values of h_1 and h_2 and a transition at h_3 that has escaped previous numerical analysis. In Fig. 5, we show ED results from calculations performed on 18- and 24-site clusters (illustrated in Fig. 2) for comparison. It can be seen that the value of h_1 obtained from ED decreases as the cluster
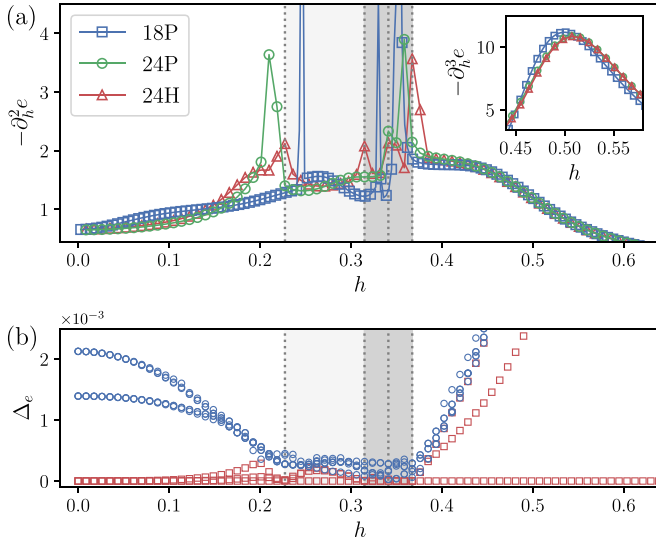
FIG. 5. (a) Energy derivatives as computed with ED on hexagonal (H) and parallelogram (P) clusters with 18 and 24 sites using PBC. Dashed lines indicate peaks in the second derivative from the 24H cluster. The intermediate phase (shaded gray) comprises regions where the ground state is singly (light gray) and multiply degenerate (dark gray). Inset: third derivative of the energy showing a smooth bump at $h \approx 0.5$. (b) Gaps to low energy states. A threefold quasidegeneracy can be distinguished within the KSL phase, with the the three lowest-energy states indicated by red squares.

size increases, moving towards the 24-site HMFT result. Moving to h_2, ED shows a series of closely spaced singularities in $\partial_h^2 e$ corresponding to a increase in ground-state degeneracy from the previously unique state, first to twofold and then to a threefold degeneracy. The extent of this degenerate region decreases with increasing cluster size, suggesting that it corresponds to the single transition seen with HMFT and DMRG [21,22]. Lastly, ED results on 18- and 24-site clusters show a peak in $\partial_h^3 e$ very close to the value of h_3 obtained from HMFT, but this peak is not accompanied by any other signature of a phase transition, including those typically appearing in the computation of fidelity susceptibility [60].

1. Intermediate phase

As mentioned previously, we find that the intermediate phase originates from a mean-field orientation with self-consistent fields that spontaneously break the $C_6 \times C_3^S$ symmetry of the Hamiltonian in favor of a reduced $C_2 \times C_1^S$ symmetry. To characterize the spontaneous symmetry breaking (SSB) found in the intermediate phase, we inspect stripe-order staggered magnetization,

$$M_{\alpha-\text{stripe}}^{\gamma} = \frac{1}{N_c} \sum_i s_i \langle S_i^{\gamma} \rangle, \qquad (8)$$

where $\alpha = x, y, z$ refers to the bond direction along which nearest neighbors are aligned and $s_i = \pm 1$ depending on which of the to two sets of stripes (with opposed spins) perpendicular to the α bonds site i belongs to (Fig. 12). In addition, to directly indicate SSB, we define an onsite observable

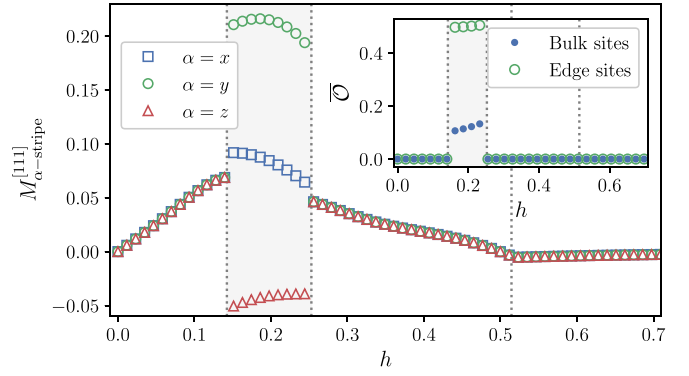$$\mathcal{O}_i = |\langle \mathbf{S}_i - \hat{U}^{-1} \mathbf{S}_i \hat{U} \rangle|, \qquad (9)$$

FIG. 6. Observables capturing the spontaneous symmetry breaking (SSB) exhibited by the intermediate phase obtained from 24-site HMFT. Main: stripe magnetizations measured along the [111] spin direction for stripes perpendicular to x, y, and z bonds. Inset: symmetry-breaking parameter (9) averaged over sites in the cluster's bulk and boundary.

where $\hat{U}$ is a unitary operator implementing a $C_6 \times C_3^S$ rotation. If $\mathcal{O}_i = 0$, then the system is symmetric. Otherwise, $\mathcal{O}_i > 0$ signals broken $C_6 \times C_3^S$ symmetry. In Fig. 6 we show stripe magnetization along the [111] direction, $M_{\alpha-\text{stripe}}^{[111]} = \frac{1}{\sqrt{3}} \sum_{\gamma} M_{\alpha-\text{stripe}}^{\gamma}$, as computed with 24-site HMFT. We find the magnetization depends on stripe direction γ only in the intermediate phase, with γ-independent values in the KSL, χ-PP, and PP phases. In particular, $M_{y\text{-stripe}}^{[111]}$ becomes dominant within the intermediate phase,[3] exceeding 20% of saturation, while the other stripe magnetizations also increase in magnitude. The dependence of stripe magnetization on γ already establishes SSB in the intermediate phase, but its presence is further supported by the nonzero values of $\mathcal{O}_i$ found in the intermediate phase. In the inset of Fig. 6, we show the average of the SSB observable Eq. (9) over the bulk and boundary (edge) sites of the cluster, with a larger value of $\mathcal{O}_i$ on cluster boundaries due to the HMFT fields. In this case, and unlike the strictly boundary mean-field order found at $h=0$, the bulk spins also exhibit SSB and acquire a nonzero stripy magnetic order. We cannot rule out that as the cluster size becomes even larger, this order vanishes as a result of finite-size scaling. Nonetheless, as we go on to show, it is clear from both HMFT and ED simulations that these stripe-order fluctuations are much stronger within the intermediate phase than in the rest of the phase diagram.

Due to the impossibility of explicit SSB in finite systems with PBC, we look for signatures of LRO in ED by computing the staggered-field susceptibility,

$$\chi_{\alpha-\text{stripe}}^{\beta\gamma} = \partial_\varepsilon \langle \Psi_\alpha^\beta(\varepsilon) | \hat{M}_{\alpha-\text{stripe}}^\gamma | \Psi_\alpha^\beta(\varepsilon) \rangle \big|_{\varepsilon=0}, \qquad (10)$$

where $|\Psi_\alpha^\beta(\varepsilon)\rangle$ is the ground state of the perturbed Hamiltonian, $H(\varepsilon) = H + \varepsilon \hat{M}_{\alpha-\text{stripe}}^\beta$, and examine the static

---

[3]The preference towards $M_{y\text{-stripe}}^{[111]}$ in particular is arbitrary, and only reflects the orientation our mean fields selected. Rotations of these fields result in an equivalent HMFT state with the same energy and a different preferred stripe orientation.
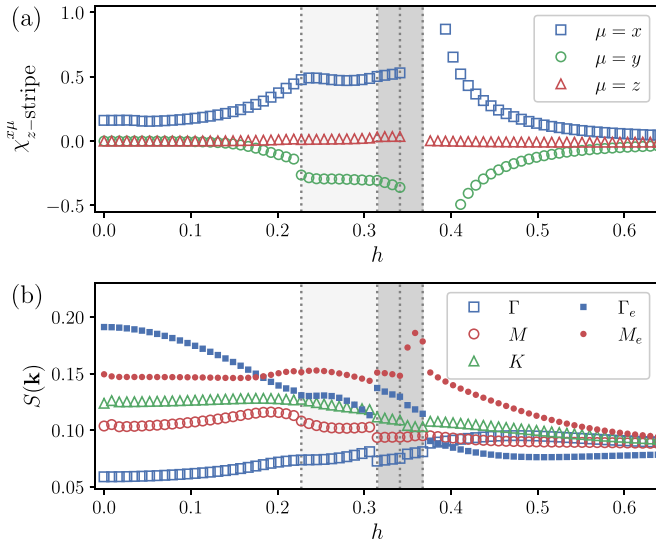
FIG. 7. (a) Staggered magnetic susceptibility (10) and (b) static structure factor (11) for different high-symmetry points of the Brillouin zone, as computed with ED on 24H cluster with PBC.

spin structure factor

$$S(\mathbf{k}) = \frac{1}{N_c^2} \sum_{i,j} e^{i\mathbf{r}_{ij}\mathbf{k}} \langle \mathbf{S}_i \mathbf{S}_j \rangle - \frac{1}{N_c} \left| \sum_i e^{i\mathbf{r}_i \cdot \mathbf{k}} \langle \mathbf{S}_i \rangle \right|^2, \qquad (11)$$

where $\mathbf{r}_{ij} = \mathbf{r}_i - \mathbf{r}_j$, at various $\mathbf{k}$-points commensurate with the 24-site honeycomb cluster (24H) and representative of various types of magnetic LRO. In particular, the points M, M_e, and Γ_e correspond to zigzag, stripe, and Néel staggered magnetizations, respectively (see Appendix E). In Fig. 7(a) we observe an increase in the magnitude of susceptibilities $\chi_{z\text{-stripe}}^{xx}$ and $\chi_{z\text{-stripe}}^{xy}$ in the intermediate phase, while $\chi_{z\text{-stripe}}^{xz}$ is near zero for all h, consistent with the presence of antiferromagnetic $\sum_{\langle ij \rangle^z} S_i^z S_j^z$ interactions in the Hamiltonian on precisely those bonds that z-direction stripes would align. In addition to the susceptibility, the static structure factor at $\mathbf{k} = M_e$, which corresponds to stripe order, is larger than at any other $\mathbf{k}$-point within the intermediate phase, as can be seen in Fig. 7(b) This is consistent with previous DMRG calculations that identified a peak at this wave vector in the intermediate phase, which has been argued to be related to the structure of a predicted spinon Fermi surface (SFS) [26]. We cannot completely rule out the possibility that the SSB we observe is an artificial signature of an otherwise SFS. However, the SSB we find in this phase is in stark disagreement with the topological state with Chern $C = 4$ predicted in basis of an effective mean-field [27] and variational Monte Carlo studies [28] and suggests that if predictions of a $C = -2$ state arising from in-plane fields [29,30] are correct, the intermediate phases caused by in-plane and out-of-plane magnetic fields are not adiabatically connected.

In the interest of further probing the putative topological nature of the intermediate phase, we calculate the many-body (MB) Chern number [52,53,55,56] on the 24H cluster in ED. This is a highly involved computation that requires integrating over a discretized torus $L \times L$ of twisted boundary conditions (TBC) [53] (see Appendix D for details). Our computations

for several TBC torus grids ($L = 6, 8, 10, 12$) indicate that the KSL and PP phases are characterized by $C = 1$ and $C = 0$, respectively, consistent with the exact limits of the KSL ($h = 0$) and PP ($K_\gamma = 0$) phases. However, we find the MB Chern number to be ill-defined within the intermediate phase, where it jumps between different integer values throughout the single ground state region, and cannot be defined for the regions where the ground state is multiply degenerate [shown as shaded dark gray in Fig. 5(b)].

Moreover, the low-energy spectrum obtained from ED simulations of the intermediate phase is inconsistent with the $C = -2$ or $C = 4$ states of Kitaev's 16-fold way [3], cases should have a fourfold degeneracy on a torus. Although in finite systems this may not manifest as an exact degeneracy [61,62], the ED spectrum obtained from the 24H cluster (Fig. 5) shows that the four lowest-energy states are not separated from the remainder of the spectrum by a gap in the intermediate phase. Instead, level crossings occur between the low-energy states and the remainder of the spectrum. In contrast, the threefold quasidegenerate ground-state manifold arising from Kitaev's exact solution [3] is preserved throughout the entire KSL phase. This clear threefold quasidegeneracy permits in addition the calculation of the topological S matrix [57], which shows good agreement between our results and the those of the exact KSL phase [23]. On the contrary, in the intermediate phase the calculation of the S matrix cannot be performed in a rigorously justified manner since the dense spectrum imposes an arbitrary choice of the ground-state manifold.[4] Among the different choices we have made, none have produced values consistent those corresponding to the $C = -2$ or $C = 4$ states of Kitaev's classification (see Appendix D for further details).

All in all, we interpret the lack of well-defined MB Chern number and distinct ground-state manifold in ED, together with the SSB signal observed in HMFT, as indications of a gapless spectrum within the intermediate phase, in agreement with previous predictions [22,23,26].

2. Chiral partially polarized phase

The combined use of spatially symmetric clusters, together with the self-consistent mean-field embedding providing information from the thermodynamic limit and allowing for the explicit breakdown of continuous symmetries, permits HMFT to discover phase transitions that may escape other methods. That is the case of the second-order phase transition we observe at $h_3 \approx 0.51$, which separates a previously unnoticed chiral region from the trivial partially polarized (PP) phase. This χ-PP phase is characterized by coexistence of partial polarization, $M^{[111]}$, and a large sublattice chirality (5), as illustrated in Fig. 4.

In Fig. 8 we perform a finite size scaling of the sublattice chirality, as computed with HMFT and ED. Within the χ-PP phase, the maximum sublattice chirality obtained from both methods exhibit a similar value of $\overline{\chi}_{\text{stag}} \approx 0.25$ on both 24H and 24P clusters, with HMFT approaching from above and ED

---

[4]Specifically, level crossings low in the spectrum means that the set of three or four states making up the putative quasidegenerate manifold are not adiabatically connected throughout the phase.
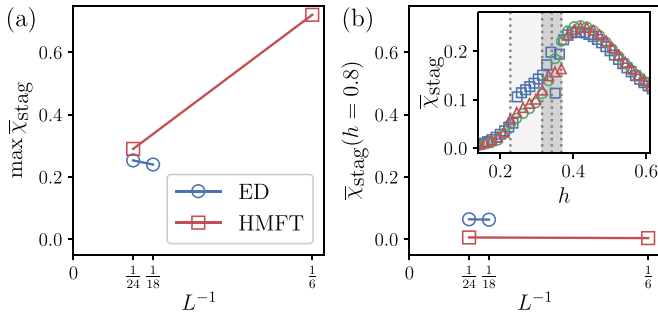
FIG. 8. (a) Finite-size scaling of maximum chirality within the χ-PP phase. ED results shown here were obtained from 18P and 24P clusters (Fig. 2) using PBC. A naive extrapolation from these results predicts a finite chirality in the thermodynamic limit from both ED and HMFT results. (b) Finite-size scaling of chirality in the PP phase at $h = 0.8$. Inset: chirality measured on 18- and 24-site clusters with PBC. Here, squares, triangles, and circles correspond to 18P, 24P, and 24H clusters.

from below. A naive linear extrapolation from Fig. 8 indicates a finite $\overline{\chi}_{\text{stag}}$ from both methods in the infinite-cluster limit. In the PP phase, both ED and HMFT show a strongly suppressed signal. Interestingly, the average chirality as computed with ED (plotted in the inset) exhibits a dependence on h close to that found in 24-site HMFT, with a maximum value at almost the same magnetic field in both 24-site ED and 18- and 24-site ED, $h \approx 0.4$.

In Fig. 9, we show that sublattice scalar chirality computed in HMFT permeates the cluster within the χ-PP phase, while in the other two nontrivial phases (KSL and intermediate) its effect is mostly present at the boundaries of the cluster only. ED calculations show uniformly staggered chirality in all phases with an increased magnitude in the χ-PP phase (see Appendix F).
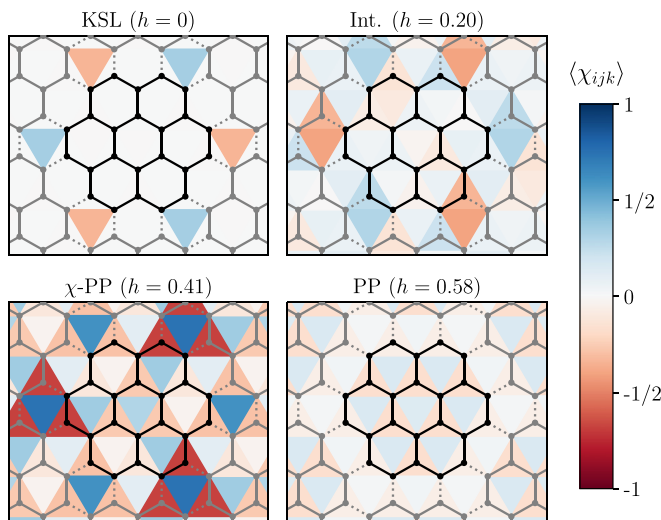

FIG. 9. Local scalar chirality [Eq. (5)] as computed with 24-site HMFT at various magnetic fields representative of the phases seen at $h > 0$. By our convention, positive (negative) values correspond to counter-clockwise (clockwise) chirality.

V. DISCUSSION AND CONCLUSION

Indications of field-revealed quantum spin liquid (QSL) behavior and topological order make frustrated magnets in the presence of external magnetic fields a subject of experimental and theoretical research attracting much attention. The exactly solvable Kitaev honeycomb model (KHM) is an important model of topological QSL physics and a potential resource for quantum computation [3], which has motivated the search for its material realization since its proposal [8,63] and extensive theoretical studies of the material-motivated extended Kitaev models [12,14,15,17–19].

In this work, we have approached the antiferromagnetic KHM by means of hierarchical mean-field theory (HMFT), a method based on the identification of relevant cluster degrees of freedom preserving symmetries of the Hamiltonian. Specifically, we have used a cluster-Gutzwiller ansatz (CGA), i.e., a simple product of uncorrelated clusters, with clusters of sizes $N_c = 6$ and 24. By these means, we compute energy and derivatives to identify quantum phase transitions, and various observables to identify spontaneous symmetry breakdown (SSB) and the potential onset of long-range order (LRO). We have supplemented these simulations with extensive exact diagonalization (ED) results, using the Lanczos algorithm to obtain the low-lying spectrum and using the resulting information to calculate the many-body Chern number. From these methods, we have found that a magnetic field in the [111] direction drives the exactly solvable Kitaev spin liquid (KSL) phase through two intermediate phases characterized by the emergence of stripe and chiral magnetic orders, respectively, before transitioning into the trivial partially polarized phase.

The HMFT ground state corresponding to the first intermediate phase is characterized by SSB and the onset of stripy magnetic order, in contrast to the gapless $U(1)$ [21–26] or gapped topological [27,28] QSLs predicted in other studies. Susceptibilities, static spin structure factors, and many-body Chern numbers calculated from ED suggest a gapless state with possible LRO. Although we cannot discard the possibility of a featureless critical state (in which case the observed SSB would be simply an artifact of the mean-field embedding), our results strongly question predictions of a gapped topological phase with a nonzero Chern number.

The second intermediate (chiral partially polarized, or χ-PP) phase is characterized by the emergence of significant sublattice chirality coexisting with partial polarization. This enhanced chirality is also observed in ED results across multiple clusters, with finite-size scaling of both HMFT and ED results indicating that the chiral order persists into the thermodynamic limit. Interestingly, this chiral phase is characterized by many-body Chern number $C = 0$. Contrary to a commonly held belief, such a Chern number can be zero in a chiral phase, as the Chern number is a unique measure of the topology of the many-body wave function [64]. It is worth noting that previous studies of the KHM with additional interaction terms have also argued for the emergence of chiral order [13,16,17]. A similar type of staggered chiral ordering, manifested as an emergent orbital magnetization in the fermionic language, has been predicted in interacting Mott insulating systems defined in triangular [59,65] and honeycomb [66] lattices.

Despite showing indications of chiral order with remarkable similarity to those seen in HMFT, ED results do not exhibit any signatures of a phase transition separating it from the trivial partially polarized (PP) phase. Although a peak is present in the third derivative of the energy at similar magnetic fields where the transition is found in HMFT, this peak is not accompanied by a gap closing. Therefore, it is possible that the observed χ-PP to PP phase transition are an artifact of HMFT and that the two phases are indeed adiabatically connected, or that the absence of this transition in ED is due simply to the small system sizes considered. Nevertheless, the robust staggered sublattice chirality observed in both ED and HMFT, together with the fact that the chirality permeates the bulk of the HMFT cluster only within the χ-PP phase, and that it does not break the model $C_6 \times C_3^S$ symmetries, indicates staggered chirality plays an important role in the physics of the Kitaev model in a range of magnetic fields above the first intermediate phase.

HMFT provides us with a broad picture of the phase diagram that can be understood as two consecutive crossing between two HMFT solutions, opening the intermediate phase, and a second-order phase transition separating the chiral and partially polarized phases, at which point these solutions become equivalent.

It is instructive to consider why our results, especially regarding SSB in the intermediate phase, were not seen in ED and DMRG studies. Unlike these methods, HMFT simultaneously considers: (i) the thermodynamic limit (as in infinite-DMRG), and (ii) the two-dimensional symmetries of the model (as in ED). Let us remark that this second aspect is key. While DMRG considers very large systems (on the order of 10^4 [22]) by simulating cylinders, the number of high-symmetry points of the Brillouin zone are the same as our 24-site cluster. Without meeting both conditions, the SSB we predict cannot be directly observed.

The CGA breaks translational invariance by construction, but provides a faithful approximation as long as the characteristic correlation length of the phase is contained within the cluster chosen. We have provided a detailed analysis of the self-consistent mean fields concomitant to the CGA and the permeability of the boundary response throughout the bulk to assess the emergence or absence of LRO in the thermodynamic limit.

To rigorously confirm the ultimate fate of the stripe order in the first intermediate phase, and the transition from the chiral order in the *exact* thermodynamic limit, clusters of sizes greater than $N_c = 24$ might be required. The resulting exponential increase of the cluster Hilbert space creates a bottleneck for standard HMFT simulations using classical computational methods. Instead, novel approaches will be required to approach larger clusters. These may utilize entanglement renormalization ideas [67], Monte Carlo methods [68,69], the use of quantum computational resources [70], or combinations thereof.
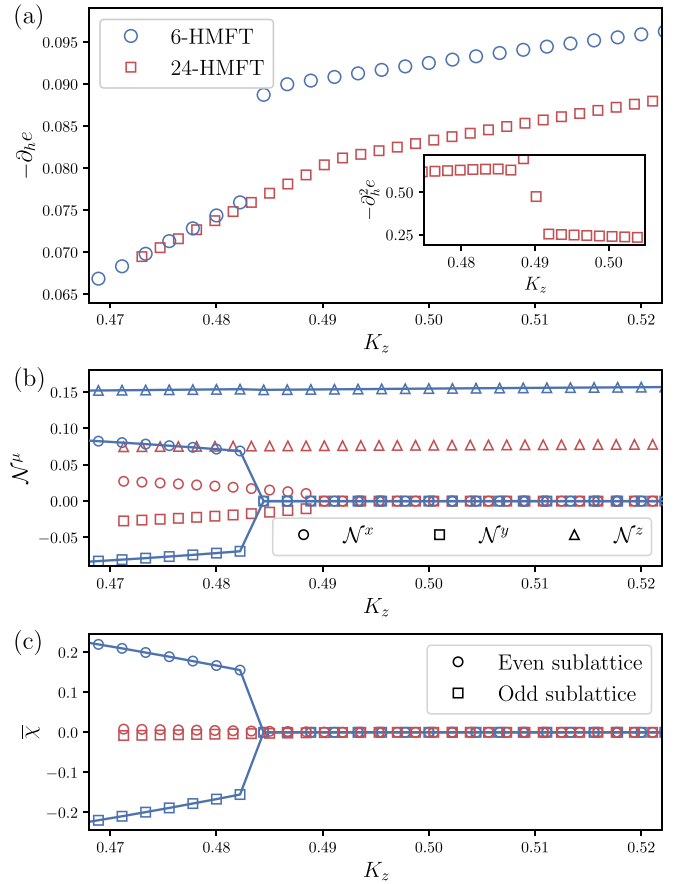
FIG. 10. Results calculated at $h = 0$ near the A_z-KSL phase transition calculated along the $K_x = K_y$ line. Blue and red symbols correspond to 6- and 24-site HMFT, respectively. 24-site results are obtained from a C_3-symmetric Néel-ordered mean field. (a) First derivative of energy density showing a discontinuity in the 6-site results and a cusp in the 24-site results. Inset: second derivative of the 24-site energy density showing a discontinuity at the transition. (b) Néel order parameter measured along x, y, and z directions. (c) Scalar chirality χ averaged over even and odd-sublattice triangles.

APPENDIX A: $h = 0$ HMFT RESULTS

To determine the HMFT phase boundaries of the Kitaev honeycomb model (KHM) at $h = 0$, we performed HMFT calculations iteratively (reusing the previous iteration's mean fields as starting parameters) moving along paths originating at the $K_x = K_z$ line and ending at the $K_z = 1$, $K_x = K_y = 0$ point, with the ratio K_x/K_y fixed on the path. These paths are illustrated in Fig. 1(a) along with the phase boundaries of the KHM from the exact solution.

Figure 10 illustrates key results from the $h=0$ calculations on the $K_x = K_y$ line [vertical in Fig. 1(a)], indicating the transition between KSL and A_z phases, occurring at $K_z = 0.5$ in the exact solution. First derivatives of the energy show a first-order transition in the 6-site HMFT results, while 24-site HMFT correctly recovers a second-order transition, with only a cusp in the first derivative [Fig. 10(a)].

Due to the HMFT mean fields, both Néel and chiral order are apparent in the HMFT solutions. The Néel order $\mathcal{N}^{\mu} = \sum_i (-1)^i \langle S_i^{\mu} \rangle$ plotted in Fig. 10(b) is illustrative of
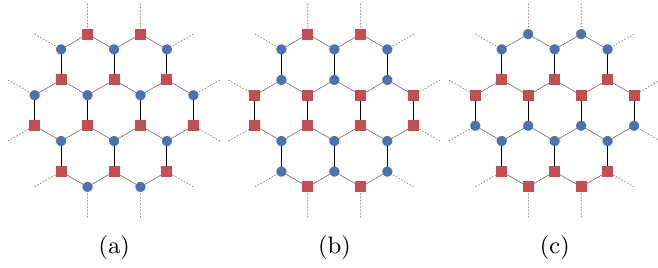
FIG. 11. Néel (a), stripe (b), and zig-zag (c) staggered magnetic orders. Rotations of the stripe and zig-zag orders give three orientations each.

the mean-field structure: in the KSL phase, Néel order exists along all spin directions. At precisely the transition into the K_z-dominated A_z phase, $\mathcal{N}^x$ and $\mathcal{N}^y$ go to zero, leaving only z-direction Néel order. This is much more visible in the 6-site results than the 24-site. Examination of the spatial dependence of spin expectation values shows that the Néel order in the 24-site cluster is only present in the boundaries (sites directly coupled to mean fields). As such, it is likely that Néel order would disappear roughly as the ratio of boundary to area of the cluster [so $\mathcal{O}(1/N_c)$] for even larger cluster sizes ($N_c > 24$). Note that this simple scaling does not apply to situations such as chirality in the χ-PP phase, where significant magnetic order exists not only at the boundaries, but within the clusters as well.

Figure 10(c) shows scalar chirality averaged over all triangles in the clusters. In the KSL phase, the even and odd sublattices acquire chirality in opposite directions, which goes to zero in the A_z phase. Again, the magnitude of chirality is much smaller in the 24-site results. In fact, the only triangles with nonzero chirality at $h=0$ are those linking three clusters (see Fig. 9). As with Néel order, we expect this indicates a strong decrease in chirality with further increases in cluster size.

Here, it should be noted that we computed observables in Fig. 10 using the C_3-symmetric Néel-ordered 24-site HMFT configuration to simplify comparison to the single (C_3-symmetric Néel-ordered) 6-site HMFT solution. The stripe-ordered solutions relevant at $h > 0$ (and degenerate at $h = 0$) replace Néel order with stripe ordering (Néel-ordered solutions have precisely zero stripe magnetization and visa-versa). Additionally, average chirality $\overline{\chi}_{\text{stag}}$ is zero in the stripe-ordered solutions, with a pattern of positive and negative chiralities throughout the cluster (see Fig. 9) resulting in an exact cancellation when summed for all couplings.

APPENDIX B: MEAN-FIELD ORIENTATIONS

Various staggered magnetizations occurring on the honeycomb lattice are shown in Fig. 11. Note that the 24-site cluster is commensurate with all three orderings, while the 6-site cluster is only commensurate with Néel order. We find self-consistent mean fields with nonzero Néel and stripe order in the 24-site cluster, while zigzag ordering is not seen for the antiferromagnetic interactions used in our simulations. Note that applying a spin flip to all even sublattice spins in the stripe-ordered arrangement transforms it to the zigzag

arrangement and visa versa. This indicates that the degeneracy between Néel and stripe order in the antiferromagnetic KHM HMFT solution corresponds to a degeneracy between zigzag and uniformly magnetized mean fields in the ferromagnetic KHM, as the models are identical up to the same sublattice spin flip.

Figure 3 shows the four categories of mean-field configurations with identical energy when $K_x = K_y = K_z = 1$ and $h = 0$. While the C_3-symmetric Néel order shown conforms to familiar Néel order where all sites on the even sublattice have $\langle S_i^\mu \rangle$ with an opposite sign to those on the odd sublattice, the other orderings are more correctly thought of as being commensurate with the labeled antiferromagnetic orders, rather than being a direct example for them. For instance, only the x-bond mean fields in the C_6-symmetric stripe orientation shown in Fig. 3 are consistent with the stripe orientation shown in Fig. 11. The y- and z-bond mean fields are consistent with other stripe orientations. As schematically illustrated in Fig. 12, these mean-field orders represent overlayed staggered magnetizations with a different ordering for each component of spin. For $h > 0$, these mean fields acquire an additional uniform magnetization skewing the mean-field values towards the [111] direction, but there is no mixture between Néel and stripy solutions at any magnetic field. This manifests as a total lack of Néel magnetic order in a stripy HMFT solution and visa versa.

APPENDIX C: CALCULATION OF MULTI-SPIN OBSERVABLES AND CORRELATORS IN HMFT

Our HMFT simulation has a wave function $|\Phi\rangle$ given by Eq. (3) that can be expressed as a tensor product of identical single-cluster wave functions $|\psi_{\mathbf{R}}\rangle$. As such, the expectation value of a multi-spin product with sites located within different clusters decomposes into the product of the expectation value within each cluster,

$$
\begin{aligned}
&\langle \Psi | S_{\mathbf{R},i}^\alpha S_{\mathbf{R},j}^\beta S_{\mathbf{R}',k}^\mu S_{\mathbf{R}'l}^\nu | \Psi \rangle \\
&\quad = \langle \psi_{\mathbf{R}} | S_{\mathbf{R},i}^\alpha S_{\mathbf{R},j}^\beta | \psi_{\mathbf{R}} \rangle \langle \psi_{\mathbf{R}'} | S_{\mathbf{R}',k}^\mu S_{\mathbf{R}'l}^\nu | \psi_{\mathbf{R}'} \rangle. \quad \text{(C1)}
\end{aligned}
$$

This decomposition is relevant for two observables we calculate: plaquette flux W_p and scalar chirality χ_{ijk}. With our 6- and 24-site clusters, these operators can occur as single-cluster, two-cluster, and three-cluster terms. To average plaquette flux and chirality, we therefore need to appropriately decompose the observable as in Eq. (C1) and then sum them with appropriate weights (1/2 for two-cluster and 1/3 for three-cluster terms) to avoid double counting terms belonging to more than one cluster. Specifically for chirality, the weights are applied as

$$
\overline{\chi}_{\text{stag}} = \frac{1}{N_c} \sum_{\substack{\langle\langle i,j,k \rangle\rangle \\ \{i,j,k\}\in\mathbf{R}}} s_{ijk}\langle \chi_{ijk}\rangle + \frac{1}{2N_c} \sum_{\substack{\langle\langle i,j,k \rangle\rangle \\ \{i,j\}\in\mathbf{R}, k\in\mathbf{R}'}} s_{ijk}\langle \chi_{ijk}\rangle
$$

$$
+ \frac{1}{3N_c} \sum_{\substack{\langle\langle i,j,k \rangle\rangle \\ i\in\mathbf{R}, j\in\mathbf{R}', k\in\mathbf{R}''}} s_{ijk}\langle \chi_{ijk}\rangle, \quad \text{(C2)}
$$

where $\langle\langle i, j, k \rangle\rangle$ refers to next-nearest-neighbor sites of the honeycomb lattice forming triangles and the first, second, and
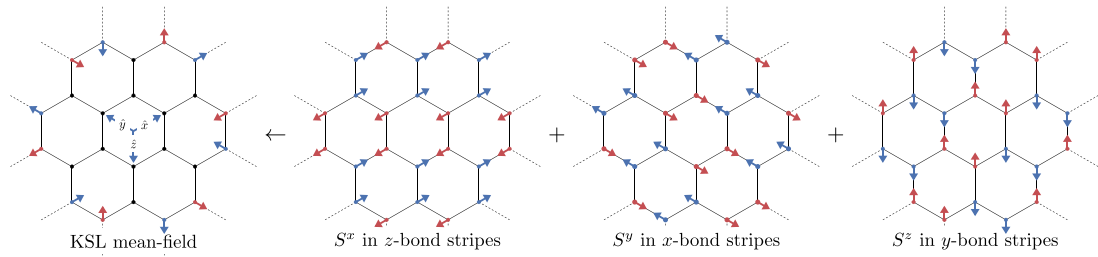
FIG. 12. Schematics of the C_6-stripy mean-field configuration describing the KSL phase as computed with 24-site HMFT. Blue (red) arrows represent positive (negative) spin along the [111] direction.

third sums corresponds to triangles with all three sites within a single cluster (at **R**), those with sites split between the cluster **R** and neighboring clusters **R**′, and those shared between three clusters (**R**, **R**′, and **R**″), respectively. The variables s_{ijk} are equal to ± 1 as introduced in Eq. (6).

Results computed using this method are shown in Fig. 4 in the main text and Fig. 10 in the preceding Appendix.

APPENDIX D: CALCULATION OF TOPOLOGICAL PROPERTIES IN ED AND HMFT

HMFT has not previously been applied to models with topological order, but our results in the KSL phase indicate the method correctly captures key topological properties of the model. As shown in Fig. 3 in the main text, at $h = 0$ we find topological entanglement entropy consistent with exact results ($S_{\text{topo}} = -\log(2)$).

In addition to topological entanglement entropy, it is possible to calculate the many-body Chern number [52,55,56] and the topological S matrix [57] from ED simulations. We are unable, however, to perform those calculations in HMFT. Techniques for computing many-body Chern number require specific (twisted) boundary conditions incompatible with the mean fields used in HMFT. To find the S matrix, linear combinations of degenerate or quasidegenerate wave functions belonging to the ground state manifold must be used, while HMFT provides access to only a single ground state. As such, we exclusively use ED to calculate these topological properties.

Details of how we obtained topological properties are illustrated in the following subsections.

1. Topological entanglement entropy

To find topological entanglement entropy S_{topo}, we take inspiration from previous work [24] in using the Kitaev-Preskill (KP) construction [50]: First, we partition our system into four mutually connected subsystems A, B, C, and D. Then, the topological entanglement entropy is given by

$$S_{\text{topo}} = S_A + S_B + S_C - S_{AB} - S_{BC} - S_{AC} + S_{ABC}, \quad \text{(D1)}$$

where S_A is the entanglement entropy acquired by tracing out degrees of freedom outside of region A, S_{AB} is the entanglement entropy acquired by tracing out degrees of freedom outside of $A \cup B$, and so on.

As this calculation occurs in the bulk of a cluster and has no reliance on boundary conditions, it can easily be performed in HMFT using the same techniques as ED, albeit with a

restricted choice of partitions as compared to what is available when periodic boundary conditions are utilized. Since HMFT breaks quantum correlations at the cluster boundaries, partitions must be chosen to connect entirely within the bulk of the cluster, as shown in Fig. 13. ED with PBC allows for larger partitions to be chosen [24].

The difference choice explains why ED finds an increase in the magnitude of S_{topo} in the intermediate phase [24], while HMFT sees only a local increase compared to immediately adjacent regions, with a maximal value much lower in magnitude than the $-\ln 2$ recovered at $h = 0$. The ED calculations are performed with larger partitions (illustrated in the supplemental material of Ref. [24]). One possibility is that the smaller partitions required by the HMFT calculation are not sufficient to accommodate an increased correlation length in the intermediate phase.

2. Topological S

The topological S matrix may be calculated in ED systems using an approach inspired by the KP topological entropy. By choosing partitions that bifurcate the cluster into disconnected regions and then finding linear combinations of the quasidegenerate ground states to extremize entanglement entropies along these partitions, the topological S matrix can be calculated via taking overlaps of these states [57]. These S matrices may also be calculated from properties of idealized topological systems, such as the categories in Kitaev's 16-fold way [3]. As such, the S matrix provides a useful quantity to
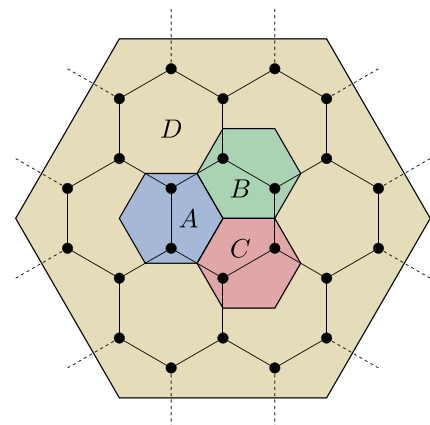

FIG. 13. Partitions used in the Kitaev-Preskill construction of the topological entanglement entropy from HMFT results.

check for correspondence between ED on finite systems and topological quantum field theory results.

This approach has already been applied to the KSL in a magnetic field, finding results in good agreement with the exact ($h = 0$) result [23]. We are able to reproduce this result over a range of magnetic fields in the KSL region using PBC on the 24H cluster. This calculation was not attempted on the 24P or 18P cluster because these clusters recover an incorrect twofold quasidegeneracy in the KSL phase rather than the required threefold quasidegeneracy.

Outside of the KSL phase, the same calculation may be performed, but with an important caveat that the ED spectrum (see Fig. 5) does not appear to exhibit the requisite topological (quasi)degeneracy in any non-KSL phase. Instead, within each phase, level crossings occur between the low-lying excited states, meaning they do not represent a topologically protected manifold. As such, the calculation is not well-motivated and the manifold of states used is arbitrary. Unsurprisingly, the S matrices thus calculated do not conform to known topological quantum field theories and change drastically within the phases at points where low-lying excited states undergo level crossings. Along with the lack of topological degeneracy, this reinforces our understanding that whatever the nature of the intermediate phase is, it is not the gapped topological system suggested in Ref. [27], which should have a well-defined S matrix given by Kitaev's 16-fold way.

3. Many-body Chern number

To calculate the many-body Chern number, twisted boundary conditions (TBC) are implemented on the 6H and 24H cluster (see Fig. 2 in main text). For spin degrees of freedom, these boundary conditions are defined as

$$S^+_{\mathbf{r}+\mathbf{L}_i} = e^{i\phi_i} S^+_{\mathbf{r}}, \tag{D2a}$$

$$S^-_{\mathbf{r}+\mathbf{L}_i} = e^{-i\phi_i} S^-_{\mathbf{r}}, \tag{D2b}$$

$$S^z_{\mathbf{r}+\mathbf{L}_i} = S^z_{\mathbf{r}}, \tag{D2c}$$

where $\mathbf{L}_i$ ($i = 1,2$) are the vectors wrapping around the torus in PBC, and ϕ_i are the phases twisting the boundary conditions. We compute the many-body Chern number using a *numerically gauge invariant* formulation, which cancels out the arbitrary $U(1)$ phase present in the many-body wave functions for each phase [52,55,56]. Specifically, we consider $L \times L$ grids of discrete phases $\phi_{1,2} \in \{0, 2\pi/L, \ldots, 2\pi(L-1)/L\}$ with $\phi = (\phi_1, \phi_2)$,

$$\widetilde{C} = \frac{1}{2\pi i} \sum_{\phi} \ln \frac{U_1(\phi) U_2(\phi + \varepsilon_1)}{U_1(\phi + \varepsilon_2) U_2(\phi)}, \tag{D3}$$

where $\varepsilon_1 = (1, 0)2\pi/L$ and $\varepsilon_2 = (0, 1)2\pi/L$, are the steps along the two directions of the $L \times L$ torus, and the variables

$$U_\mu = \frac{\langle \Psi(\phi) | \Psi(\phi + \varepsilon_\mu) \rangle}{|\langle \Psi(\phi) | \Psi(\phi + \varepsilon_\mu) \rangle|} \tag{D4}$$

are defined at each point on the grid with $|\Psi(\phi)\rangle$ indicating the ground state of the Hamiltonian at each TBC, ϕ. Even for very coarse grids (small L), this formulation returns well-quantized integers, and for large enough L, $\widetilde{C}$ corresponds to the many-body Chern number in the continuum, C [55,56].
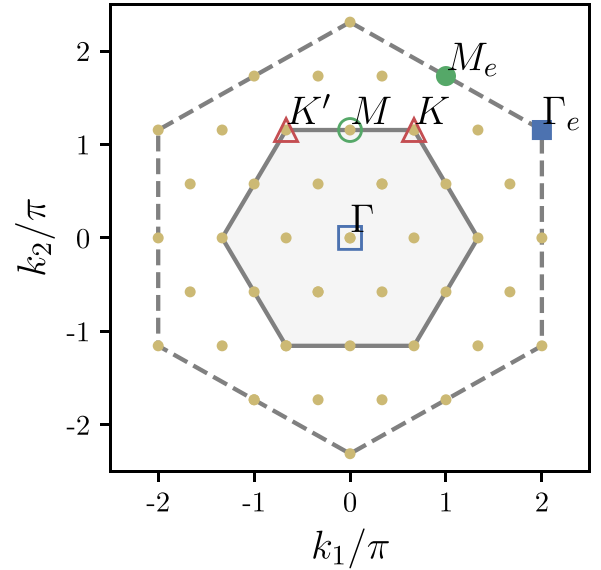

FIG. 14. Extended Brillouin zone of the honeycomb lattice showing points commensurate with the 24H cluster. Γ, K, K', and Γ_e points are also commensurate with the 6-site cluster, while the other points (crucially, M and M_e) are not. Labels correspond to the same points utilized in Fig. 15.

Notice that the many-body Chern number is a quite involved computation, as it requires performing exact diagonalization at each point of the grid.

We use $L = 6$, 8, 10, and 12 TBC grids, and find $C = 1$ within the KSL phase, consistent with exact results [3]. The PP phase is characterized by $C = 0$, consistently with trivial Landau order. As PP and χ-PP phases are adiabatically connected in ED (i.e., absence of gap closing), we also obtain $C = 0$ in the χ-PP phase. Notice that while *vector* chiral order is usually accompanied by a nonzero Chern number, the χ-PP phase found is characterized by *scalar* chirality.

In the intermediate phase, where the low-energy ED spectrum is denser (see Fig. 5 in main text), we obtain a Chern number that varies with h, jumping between different integers (within working numerical precision) and changing drastically with changing grid sizes. On the 18P cluster, whose smaller Hilbert space allows for much quicker calculations, even very fine grids (20×20) did not resolve these jumps in Chern number. These phenomena may be interpreted as an indication of gaplessness in the thermodynamic limit, which would prevent measurement of the Chern number.

Finally, notice that although the KHM does not display a $U(1)$ symmetry, computation of the many-body Chern number, by realizing a $U(1)$ bundle using TBC from Eq. (D2), leads to the exact nontrivial $C=1$ result in the KSL phase, as well as the $C=0$ in the trivial PP phase.

APPENDIX E: BRILLOUIN ZONE OF THE HONEYCOMB LATTICE

The honeycomb lattice is not a Bravais lattice. Rather, it consists of a triangular (Bravais) lattice of two-site unit cells. Because of this, some properties of the reciprocal lattice can be counterintuitive.
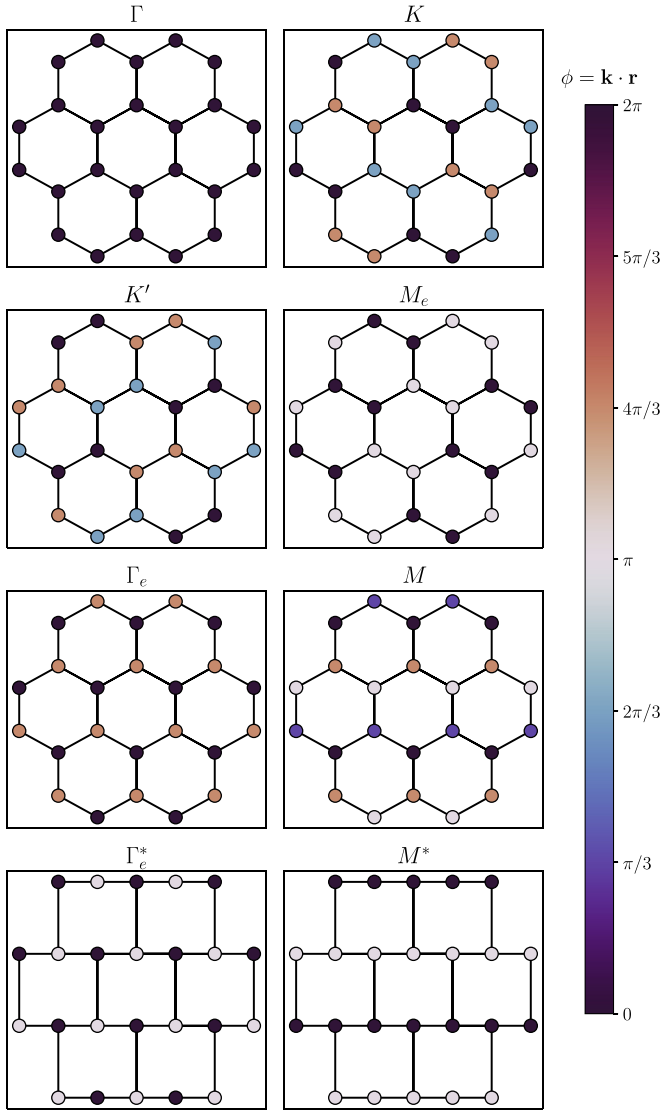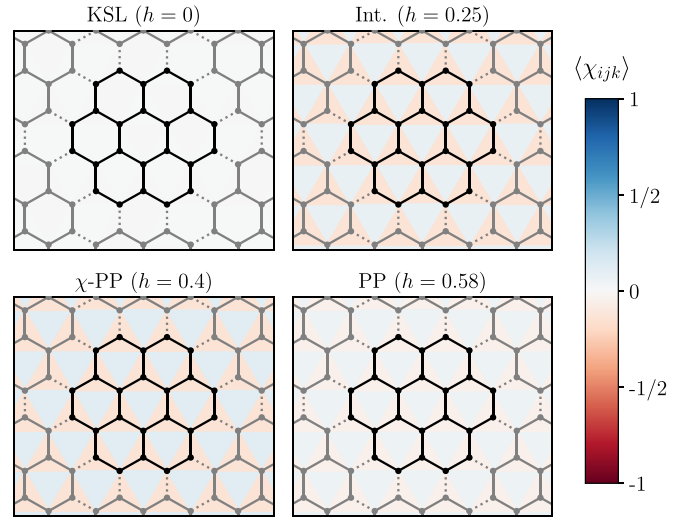
FIG. 16. Chirality [Eq. (5)] computed on the 24H cluster with PBC at various magnetic fields. By our convention, positive (negative) values correspond to counter-clockwise (clockwise) chiral currents.

FIG. 15. Phase $\phi = \mathbf{r} \cdot \mathbf{k}$ at each point in the 24-site cluster for various $\mathbf{k}$ corresponding to different local orders. The M and Γ_e plots are plotted on both honeycomb and brickwall lattices (M^*, Γ_e^*). Note that only on the brickwall lattice do these wave vectors produce the π relative phases corresponding to zigzag and Néel order.

We can construct the honeycomb lattice with unit cell translation vectors

$$\mathbf{a}_1 = \frac{a}{2}\begin{pmatrix} 1 \\ \sqrt{3} \end{pmatrix}, \quad \mathbf{a}_2 = \frac{a}{2}\begin{pmatrix} -1 \\ \sqrt{3} \end{pmatrix}, \quad \text{(E1)}$$

which have corresponding reciprocal lattice vectors

$$\mathbf{b}_1 = 2\pi\begin{pmatrix} 1 \\ 1/\sqrt{3} \end{pmatrix}, \quad \mathbf{b}_2 = 2\pi\begin{pmatrix} -1 \\ 1/\sqrt{3} \end{pmatrix}. \quad \text{(E2)}$$

The vectors $\mathbf{a}_i$ connect next-nearest neighbors (sites belonging to the same triangular sublattice). To complete the honeycomb lattice, we require a third vector to connect sites of opposite sublattices. One choice is

$$\mathbf{a}_3 = \frac{1}{\sqrt{3}}\begin{pmatrix} 0 \\ 1 \end{pmatrix}. \quad \text{(E3)}$$

Because of this structure within unit cells, points in $\mathbf{k}$-space outside of the first Brillouin zone (BZ) of the underlying triangular lattice correspond to different phases $\mathbf{r} \cdot \mathbf{k}$, and therefore have different physical meaning. As such, we construct the *extended Brillouin zone* to accommodate these additional points. This extended BZ is depicted in Fig. 14, with high-symmetry points labeled (and with a subscript e indicating points outside the first BZ).

Figure 15 shows the phase $\mathbf{r} \cdot \mathbf{k}$ acquired at each point in the 24H cluster at high-symmetry wave vector. From this, it is clear that the Γ wave vector corresponds to a uniform magnetization (as expected) and M_e forms stripe order (along y bonds in this case, with the different M_e points resulting in different stripe orientations).

However, the Γ_e point on the honeycomb lattice has nearest-neighbor spins acquiring a relative phase of $2\pi/3$. If this phase were instead π, then this would correspond to Néel order. Surprisingly, no single wave vector on the honeycomb lattice assigns a relative π phase to nearest neighbors. Instead, to find wave vector corresponding to Néel order, we deform the honeycomb lattice into the topologically equivalent brickwall lattice (as in the lowest two subplots in Fig. 15). Under such a deformation, the Γ_e point does correspond to Néel order. Similarly, the M points go from producing a variety of relative phases on the honeycomb lattice to producing a π relative phase on sites corresponding to zigzag order on the brickwall lattice. For this reason, the structure factors $S(M)$ and $S(\Gamma_e)$ plotted in Fig. 7(b) were computed on the brickwall lattice.

APPENDIX F: SCALAR CHIRALITY IN EXACT-DIAGONALIZATION

Figure 16 illustrates the distribution of scalar chirality from ED, similarly to the HMFT results shown in the main text

(Fig. 9). Due to the periodic boundary conditions (and therefore, translational invariance) of the simulation, chirality from ED is evenly distributed, with a distinction only between site and hexagon-centered triangles.

[1] J. Knolle and R. Moessner, A field guide to spin liquids, Annu. Rev. Condens. Matter Phys. **10**, 451 (2019).

[2] L. Savary and L. Balents, Quantum spin liquids: A review, Rep. Prog. Phys. **80**, 016502 (2017).

[3] A. Kitaev, Anyons in an exactly solved model and beyond, Ann. Phys. **321**, 2 (2006).

[4] Z. Nussinov and G. Ortiz, Bond algebras and exact solvability of Hamiltonians: Spin $S = \frac{1}{2}$ multilayer systems, Phys. Rev. B **79**, 214440 (2009).

[5] K. W. Plumb, J. P. Clancy, L. J. Sandilands, V. V. Shankar, Y. F. Hu, K. S. Burch, H.-Y. Kee, and Y.-J. Kim, α-RuCl$_3$: A spin-orbit assisted Mott insulator on a honeycomb lattice, Phys. Rev. B **90**, 041112(R) (2014).

[6] J. A. Sears, M. Songvilay, K. W. Plumb, J. P. Clancy, Y. Qiu, Y. Zhao, D. Parshall, and Y.-J. Kim, Magnetic order in α-RuCl$_3$: A honeycomb-lattice quantum magnet with strong spin-orbit coupling, Phys. Rev. B **91**, 144420 (2015).

[7] L. J. Sandilands, Y. Tian, K. W. Plumb, Y.-J. Kim, and K. S. Burch, Scattering continuum and possible fractionalized excitations in α-RuCl$_3$, Phys. Rev. Lett. **114**, 147201 (2015).

[8] J. C. V. Chaloupka, G. Jackeli, and G. Khaliullin, Kitaev-Heisenberg model on a honeycomb lattice: Possible exotic phases in iridium oxides A_2IrO$_3$, Phys. Rev. Lett. **105**, 027204 (2010).

[9] H.-S. Kim and H.-Y. Kee, Crystal structure and magnetism in α-RuCl$_3$: An *ab initio* study, Phys. Rev. B **93**, 155143 (2016).

[10] L. Janssen, E. C. Andrade, and M. Vojta, Magnetization processes of zigzag states on the honeycomb lattice: Identifying spin models for α-RuCl$_3$ and Na$_2$IrO$_3$, Phys. Rev. B **96**, 064430 (2017).

[11] S. Trebst and C. Hickey, Kitaev materials, Phys. Rep. **950**, 1 (2022).

[12] L. Janssen, E. C. Andrade, and M. Vojta, Honeycomb-lattice Heisenberg-Kitaev model in a magnetic field: Spin canting, metamagnetism, and vortex crystals, Phys. Rev. Lett. **117**, 277202 (2016).

[13] Z.-X. Liu and B. Normand, Dirac and chiral quantum spin liquids on the honeycomb lattice in a magnetic field, Phys. Rev. Lett. **120**, 187201 (2018).

[14] J. S. Gordon, A. Catuneanu, E. S. Sørensen, and H.-Y. Kee, Theory of the field-revealed Kitaev spin liquid, Nat. Commun. **10**, 2019 (2019).

[15] W. Yang, A. Nocera, T. Tummuru, H.-Y. Kee, and I. Affleck, Phase diagram of the spin-1/2 Kitaev-Gamma chain and emergent SU(2) symmetry, Phys. Rev. Lett. **124**, 147205 (2020).

[16] A. Ralko and J. Merino, Novel chiral quantum spin liquids in Kitaev magnets, Phys. Rev. Lett. **124**, 217203 (2020).

[17] E. S. Sørensen, A. Catuneanu, J. S. Gordon, and H.-Y. Kee, Heart of entanglement: Chiral, nematic, and incommensurate phases in the Kitaev-Gamma ladder in a field, Phys. Rev. X **11**, 011013 (2021).

[18] W. Yang, A. Nocera, E. S. Sørensen, H.-Y. Kee, and I. Affleck, Classical spin order near the antiferromagnetic Kitaev point in the spin-$\frac{1}{2}$ Kitaev-Gamma chain, Phys. Rev. B **103**, 054437 (2021).

[19] S.-S. Zhang, G. B. Halász, W. Zhu, and C. D. Batista, Variational study of the Kitaev-Heisenberg-Gamma model, Phys. Rev. B **104**, 014411 (2021).

[20] F. Yilmaz, A. P. Kampf, and S. K. Yip, Phase diagrams of Kitaev models for arbitrary magnetic field orientations, Phys. Rev. Res. **4**, 043024 (2022).

[21] Z. Zhu, I. Kimchi, D. N. Sheng, and L. Fu, Robust non-Abelian spin liquid and a possible intermediate phase in the antiferromagnetic Kitaev model with magnetic field, Phys. Rev. B **97**, 241110(R) (2018).

[22] M. Gohlke, R. Moessner, and F. Pollmann, Dynamical and topological properties of the Kitaev model in a [111] magnetic field, Phys. Rev. B **98**, 014418 (2018).

[23] C. Hickey and S. Trebst, Emergence of a field-driven $U(1)$ spin liquid in the Kitaev honeycomb model, Nat. Commun. **10**, 530 (2019).

[24] D. C. Ronquillo, A. Vengal, and N. Trivedi, Signatures of magnetic-field-driven quantum phase transitions in the entanglement entropy and spin dynamics of the Kitaev honeycomb model, Phys. Rev. B **99**, 140413(R) (2019).

[25] S. Pradhan, N. D. Patel, and N. Trivedi, Two-magnon bound states in the Kitaev model in a [111] field, Phys. Rev. B **101**, 180401(R) (2020).

[26] N. D. Patel and N. Trivedi, Magnetic field-induced intermediate quantum spin liquid with a spinon Fermi surface, Proc. Natl. Acad. Sci. USA **116**, 12199 (2019).

[27] S.-S. Zhang, G. B. Halász, and C. D. Batista, Theory of the Kitaev model in a [111] magnetic field, Nat. Commun. **13**, 399 (2022).

[28] M.-H. Jiang, S. Liang, W. Chen, Y. Qi, J.-X. Li, and Q.-H. Wang, Tuning topological orders by a conical magnetic field in the Kitaev model, Phys. Rev. Lett. **125**, 177203 (2020).

[29] J. Nasu, Y. Kato, Y. Kamiya, and Y. Motome, Successive Majorana topological transitions driven by a magnetic field in the Kitaev model, Phys. Rev. B **98**, 060416(R) (2018).

[30] S. Liang, M.-H. Jiang, W. Chen, J.-X. Li, and Q.-H. Wang, Intermediate gapless phase and topological phase transition of the Kitaev model in a uniform magnetic field, Phys. Rev. B **98**, 054433 (2018).

[31] G. Ortiz and C. D. Batista, Hierarchical mean-field theory in quantum statistical mechanics: A bosonic example, Phys. Rev. B **67**, 134301 (2003).

[32] G. Ortiz and C. D. Batista, in *Condensed Matter Theories* (Nova Science Publishers, Huntington, New York, 2003), Vol. 18, pp. 225–234.

[33] G. Ortiz and C. D. Batista, Hierarchical mean-field theories, arXiv:cond-mat/0403222.

[34] L. Isaev, G. Ortiz, and J. Dukelsky, Hierarchical mean-field approach to the J_1-J_2 Heisenberg model on a square lattice, Phys. Rev. B **79**, 024409 (2009).

[35] L. Isaev, G. Ortiz, and J. Dukelsky, Local physics of magnetization plateaux in the Shastry-Sutherland model, Phys. Rev. Lett. **103**, 177201 (2009).

[36] D. Huerga, J. Dukelsky, N. Laflorencie, and G. Ortiz, Chiral phases of two-dimensional hard-core bosons with frustrated ring exchange, Phys. Rev. B **89**, 094401 (2014).

[37] D. Huerga, S. Capponi, J. Dukelsky, and G. Ortiz, Staircase of crystal phases of hard-core bosons on the kagome lattice, Phys. Rev. B **94**, 165124 (2016).

[38] R. Okuma, D. Nakamura, T. Okubo, A. Miyake, A. Matsuo, K. Kindo, M. Tokunaga, N. Kawashima, S. Takeyama, and Z. Hiroi, A series of magnon crystals appearing under ultrahigh magnetic fields in a kagomé antiferromagnet, Nat. Commun. **10**, 1229 (2019).

[39] D. C. Ronquillo, Magnetic-field-driven quantum phase transitions of the Kitaev honeycomb model, Ph.D. thesis, Ohio State University, 2020.

[40] C. D. Batista and G. Ortiz, Algebraic approach to interacting quantum systems, Adv. Phys. **53**, 1 (2004).

[41] G. Evenbly and G. Vidal, Algorithms for entanglement renormalization, Phys. Rev. B **79**, 144108 (2009).

[42] L. Tagliacozzo, G. Evenbly, and G. Vidal, Simulation of two-dimensional quantum systems using a tree tensor network that exploits the entropic area law, Phys. Rev. B **80**, 235127 (2009).

[43] C. Lacroix, P. Mendels, and F. Mila, *Introduction to Frustrated Magnetism: Materials, Experiments, Theory*, Springer Series in Solid-State Sciences (Springer, Berlin, 2011).

[44] P. Henelius and A. W. Sandvik, Sign problem in Monte Carlo simulations of frustrated quantum spin systems, Phys. Rev. B **62**, 1102 (2000).

[45] M. Marvian, D. A. Lidar, and I. Hen, On the computational complexity of curing non-stochastic Hamiltonians, Nat. Commun. **10**, 1571 (2019).

[46] S. Greschner, D. Huerga, G. Sun, D. Poletti, and L. Santos, Density-dependent synthetic magnetism for ultracold atoms in optical lattices, Phys. Rev. B **92**, 115120 (2015).

[47] D. Huerga, J. Dukelsky, and G. E. Scuseria, Composite boson mapping for lattice boson systems, Phys. Rev. Lett. **111**, 045701 (2013).

[48] L. Isaev and G. Ortiz, Frustrated magnets and quantum paramagnetic phases at finite temperature, Phys. Rev. B **86**, 100402(R) (2012).

[49] D. Huerga, A. Greco, C. Gazza, and A. Muramatsu, Translation-invariant parent Hamiltonians of valence bond crystals, Phys. Rev. Lett. **118**, 167202 (2017).

[50] A. Kitaev and J. Preskill, Topological entanglement entropy, Phys. Rev. Lett. **96**, 110404 (2006).

[51] P. Weinberg and M. Bukov, QuSpin: A Python package for dynamics and exact diagonalisation of quantum many body systems part I: Spin chains, SciPost Phys. **2**, 003 (2017).

[52] G. Ortiz and R. M. Martin, Macroscopic polarization as a geometric quantum phase: Many-body formulation, Phys. Rev. B **49**, 14202 (1994).

[53] F. D. M. Haldane and D. P. Arovas, Quantized spin currents in two-dimensional chiral magnets, Phys. Rev. B **52**, 4223 (1995).

[54] G. Ortiz, P. Ordejón, R. M. Martin, and G. Chiappe, Quantum phase transitions involving a change in polarization, Phys. Rev. B **54**, 13515 (1996).

[55] T. Fukui, Y. Hatsugai, and H. Suzuki, Chern numbers in discretized Brillouin zone: Efficient method of computing (spin) Hall conductances, J. Phys. Soc. Jpn. **74**, 1674 (2005).

[56] C. N. Varney, K. Sun, M. Rigol, and V. Galitski, Topological phase transitions for interacting finite systems, Phys. Rev. B **84**, 241105(R) (2011).

[57] Y. Zhang, T. Grover, A. Turner, M. Oshikawa, and A. Vishwanath, Quasiparticle statistics and braiding from ground-state entanglement, Phys. Rev. B **85**, 235151 (2012).

[58] M. Hermanns, I. Kimchi, and J. Knolle, Physics of the Kitaev model: Fractionalization, dynamic correlations, and material connections, Annu. Rev. Condens. Matter Phys. **9**, 17 (2018).

[59] K. A. Al-Hassanieh, C. D. Batista, G. Ortiz, and L. N. Bulaevskii, Field-induced orbital antiferromagnetism in Mott insulators, Phys. Rev. Lett. **103**, 216402 (2009).

[60] A. F. Albuquerque, F. Alet, C. Sire, and S. Capponi, Quantum critical scaling of fidelity susceptibility, Phys. Rev. B **81**, 064418 (2010).

[61] X. G. Wen and Q. Niu, Ground-state degeneracy of the fractional quantum Hall states in the presence of a random potential and on high-genus Riemann surfaces, Phys. Rev. B **41**, 9377 (1990).

[62] Y. Hatsugai, Characterization of topological insulators: Chern numbers for ground state multiplet, J. Phys. Soc. Jpn. **74**, 1374 (2005).

[63] G. Jackeli and G. Khaliullin, Mott insulators in the strong spin-orbit coupling limit: From Heisenberg to a quantum compass and Kitaev models, Phys. Rev. Lett. **102**, 017205 (2009).

[64] C. Waldtmann, H. U. Everts, B. Bernu, C. Lhuillier, P. Sindzingre, P. Lecheminant, and L. Pierre, First excitations of the spin 1/2 Heisenberg antiferromagnet on the kagomé lattice, Eur. Phys. J. B **2**, 501 (1998).

[65] L. N. Bulaevskii, C. D. Batista, M. V. Mostovoy, and D. I. Khomskii, Electronic orbital currents and polarization in Mott insulators, Phys. Rev. B **78**, 024402 (2008).

[66] S. Banerjee and S.-Z. Lin, Emergent orbital magnetization in Kitaev quantum magnets, SciPost Phys. **14**, 127 (2023).

[67] G. Vidal, Entanglement renormalization, Phys. Rev. Lett. **99**, 220405 (2007).

[68] A. Honecker, S. Wessel, R. Kerkdyk, T. Pruschke, F. Mila, and B. Normand, Thermodynamic properties of highly frustrated quantum spin ladders: Influence of many-particle bound states, Phys. Rev. B **93**, 054408 (2016).

[69] F. Alet, K. Damle, and S. Pujari, Sign-problem-free Monte Carlo simulation of certain frustrated quantum magnets, Phys. Rev. Lett. **117**, 197203 (2016).

[70] D. Huerga, Variational quantum simulation of valence-bond solids, Quantum **6**, 874 (2022).